GTC Simulation of Ideal Ballooning Mode in Tokamak Plasmas*

LI Zebin (李泽彬)[1], SUN Guoya (孙国亚)[1], Ihor HOLOD[2], XIAO Yong (肖湧)[3], ZHANG Wenlu (张文禄)[4], LIN Zhihong (林志宏)[2,5]

[1]Department of Physics, and Institute of Theoretical Physics and Astrophysics, Xiamen University, Xiamen 361005, China
[2]Department of Physics and Astronomy, University of California, Irvine, California 92697, USA
[3]Institute of Fusion Theory and Simulation, Zhejiang University, Hangzhou 310027, China
[4]CAS Key Laboratory of Basic Plasma Physics, University of Science and Technology of China, Hefei 230026, China
[5]Fusion Simulation Center, Peking University, Beijing 100871, China

Abstract In the present paper, we first derive the eigenmode equation of the ideal ballooning mode in tokamak plasmas using a gyrokinetic equation. It is shown that the gyrokinetic eigenmode equation can be reduced to the magnetohydrodynamic (MHD) form in the long wavelength limit when kinetic effects are ignored. Then, the global gyrokinetic toroidal code (GTC) is applied for simulations of the edge-localized ideal ballooning modes. The obtained mode structures are compared with the results of ideal MHD simulations. The observed scaling of the linear growth rate with the toroidal mode number is consistent with the ideal MHD theory. The simulation results verify the GTC capability of simulating MHD processes in toroidal plasmas.

Keywords: edge-localized ideal ballooning mode, global gyrokinetic toroidal code, tokamak plasmas

PACS: *52.55.Fa, 52.35.Py, 52.65.Tt*

DOI: 10.1088/1009-0630/15/6/03

1 Introduction

The performance of tokamaks and other magnetic fusion devices depends crucially on the dynamics of the boundary region, i.e., the transition region from the hot core plasma through the edge to the material surface of the first wall [1]. The plasma boundary region has a number of physics attributes which make it quite distinct from the core: relatively low temperature, large radial gradients, and high neutral-gas and impurity densities. The large radial gradients of pressure tend to drive an edge turbulence stronger than the core turbulence in terms of the density fluctuation as a percentage of the equilibrium value [2].

It has long been known that edge fluctuations in tokamak plasmas are large, and that these fluctuations are related to the degradation of overall confinement [3]. Over the years, many unstable modes have been studied in order to explain these fluctuations. It has been shown that the rippling mode [4] and the microtearing mode [5] will not play a role in driving such fluctuations. However, there remain other modes that are yet to be fully understood [6]. Edge localized modes (ELMs) and the edge pedestal are key issues in fusion plasmas, and ELMs have been routinely observed in tokamak plasma operating in a high confinement mode (H-mode). The planned ITER device will require both a relatively high pedestal and the avoidance of large ELMs for optimal performance [7]. ELM onsets are typically associated with the crossing of plasma instability boundaries. The ideal ballooning mode, kinetic ballooning mode and peeling ballooning mode are regarded as important candidates for ELMs. These edge localized instabilities are driven by the large pressure gradient and edge currents. Pressure gradients drive ballooning instabilities while edge currents drive peeling modes [8]. There have been some successes in explaining ELMs and pedestal constraints using the peeling-ballooning modes in recent years [7].

At sufficiently large values of the plasma pressure, the pressure gradient may become large enough to produce a "ballooning" instability in regions of bad curvature in a tokamak. Ballooning modes are generally categorized as being either resistive or ideal, depending on whether the electron motion parallel to the field is impeded by collision or induction.

Most previous efforts to investigate the properties of the ideal ballooning mode (IBM) are magnetohydrodynamic (MHD) simulations, which do not treat kinetic effects. In reality, kinetic effects can modify the properties of the modes by finite Larmor radial effects and wave-particle resonances. These kinetic effects can be effectively treated in gyrokinetic simulation. Gyrokinetic particle simulation is a powerful and reliable tool for describing plasma turbulence and transport [9], and can be applied to study the ballooning mode evolution

*supported by U. S. Department of Energy (DOE) SciDAC GSEP Center and National Special Research Program of China for ITER

and turbulent transport. In the present paper, we report the progress in this direction using the global gyrokinetic toroidal code (GTC) [10] for simulations of the ideal ballooning modes in toroidally confined plasmas.

The gyrokinetic toroidal code (GTC) is a well benchmarked full torus particle-in-cell code for simulations of multiple physics processes including microturbulence, energetic particle physics, and kinetic modes in fusion plasmas. A fluid-kinetic hybrid electron model that overcomes the numerical difficulty for simultaneously treating the dynamics of ions and electrons has been developed based on an expansion of the electron response using the electron-ion mass ratio as a small parameter [11]. A nonlinear gyrokinetic simulation model incorporating an equilibrium current has been formulated for studying kinetic-MHD processes in magnetized plasmas [12]. This complete formulation enables the gyrokinetic simulation of both pressure-gradient-driven and current-driven instabilities as well as their nonlinear interactions in multiscale simulations. The gyrokinetic simulation model recovers the ideal MHD theory in the linear long wavelength regime including ideal and kinetic ballooning modes, kink modes and shear Alfven waves. The implementation of this model in the global gyrokinetic particle code has been verified for the simulation of the effects of equilibrium current on the reversed shear Alfven eigenmode in tokamaks. A single GTC version is capable of both full-f and δf simulations, kinetic electrons and electromagnetic fluctuations, general toroidal geometry and experimental plasma profiles, multiple ion species, neoclassical effects with Fokker-Planck collision operators, equilibrium current and radial electric field, plasma rotations, sources/sinks and external antenna. GTC has recently been applied to simulate the Alfven eigenmode in a tokamak [12~15]. Simulation of the edge-localized ideal ballooning mode instability using global gyrokinetic toroidal code GTC is presented. The obtained mode structure is compared with the results of ideal MHD simulations. The observed scaling of the linear growth rate with the toroidal mode number is consistent with the ideal MHD theory. The simulation results verify the GTC capability of simulating MHD processes in toroidal plasma.

This paper is organized as follows. The simulation model and formulation of the ideal ballooning mode is described in section 2. In section 3, the simulation results are presented, and some comparisons will be made against the results of ideal MHD codes simulation. Section 4 is the conclusion.

2 Model and formulation

We start by describing the electromagnetic simulation model used in the GTC code. In gyrokinetic particle simulations, the plasma is treated as a set of marker particles interacting with each other through self-generated electromagnetic fields. The field equations are discretized on the three-dimensional spatial grids of a field-aligned mesh, and the particle equations of motion are formulated in the magnetic coordinates. Electromagnetic simulations are computationally more challenging, compared to the electrostatic simulations, due to the required resolution of the fast electron dynamics and the calculation of higher velocity moments of the particle distribution function.

The gyrokinetic equation describing plasmas in the inhomogeneous magnetic field, using the gyrocenter position $\mathbf{X}$, magnetic moment μ, and parallel velocity $v_\parallel$ as a set of independent variables in the five dimensional phase space, reads [16]

$$\frac{\mathrm{d}}{\mathrm{d}t}f_\alpha\left(\mathbf{X},\mu,v_\parallel,t\right)\equiv\left[\frac{\partial}{\partial t}+\dot{\mathbf{X}}\cdot\nabla+\dot{v_\parallel}\frac{\partial}{\partial v_\parallel}-C_\alpha\right]f_\alpha=0, \tag{1}$$

$$\dot{\mathbf{X}}=v_\parallel\frac{\mathbf{B}}{B_0}+\mathbf{v}_E+\mathbf{v}_\mathrm{d}, \tag{2}$$

$$\dot{v_\parallel}=-\frac{1}{m_\alpha}\frac{\mathbf{B}^*}{B_0}\cdot(\mu\nabla B_0+Z_\alpha\nabla\phi)-\frac{Z_\alpha}{m_\alpha c}\frac{\partial A_\parallel}{\partial t}. \tag{3}$$

Here index $\alpha=e,i$ stands for the particle species (electron or ion), C_α is the collision term, omitted from now on for collisionless plasmas. m_α and Z_α are the particle charge and particle mass, respectively. $\mathbf{B}\equiv B_0\mathbf{b}_0$ is the equilibrium magnetic field, $\mathbf{B}=\mathbf{B}_0+\delta\mathbf{B}$, with $\delta\mathbf{B}=\nabla\times\delta\mathbf{A}$ being the perturbed one. $\mathbf{B}^*$ is given by

$$\mathbf{B}^*=\mathbf{B}_0^*+\delta\mathbf{B}=\mathbf{B}_0+\frac{B_0v_\parallel}{\Omega_\alpha}\nabla\times\mathbf{b}_0+\delta\mathbf{B}. \tag{4}$$

Other terms in Eq. (2) are the $\mathbf{E}\times\mathbf{B}$ drift velocity,

$$\mathbf{v}_E=\frac{c\mathbf{b}_0\times\nabla\phi}{B_0}, \tag{5}$$

and the magnetic drift velocity,

$$\mathbf{v}_\mathrm{d}=\mathbf{v}_\mathrm{c}+\mathbf{v}_\mathrm{g}, \tag{6}$$

with magnetic curvature drift $\mathbf{v}_\mathrm{c}$ and grad-B drift $\mathbf{v}_\mathrm{g}$ given as,

$$\mathbf{v}_\mathrm{c}=\frac{v_\parallel^2}{\Omega_\alpha}\nabla\times\mathbf{b}_0, \tag{7}$$

$$\mathbf{v}_\mathrm{g}=\frac{\mu}{m_\alpha\Omega_\alpha}\mathbf{b}_0\times\nabla\mathbf{B}_0, \tag{8}$$

respectively.

To simulate the electron dynamics, the fluid-kinetic hybrid electron model [11,17~19] is adopted, which is built upon the expansion of the electron response into the lowest order adiabatic part and a higher-order kinetic response, based on the electron-ion mass ratio as a small parameter. With this fluid-kinetic hybrid electron model, the nonresonant current is fully retained in the fluid equations with no need to resolve the individual particle dynamics of these nonresonant electrons. Meanwhile, the wave-particle resonances and the nonadiabatic response of magnetically trapped electrons are recovered by the higher order kinetic correction.

In this paper, only the lowest order electron density response is considered, described by the linear fluid continuity equation. Extension of the continuity equation to include nonlinear terms and equilibrium current

is described in Ref. [12]. Integrating Eq. (1), keeping terms up to the first order in the perturbation, and assuming zero equilibrium plasma current, $\nabla \times \mathbf{B}_0 = 0$, we get the continuity equations for the electron and ion density as,

$$\frac{\partial n_\mathrm{e}}{\partial t} + \mathbf{B}_0 \cdot \nabla \left(\frac{n_{0\mathrm{e}} \delta u_{\parallel \mathrm{e}}}{B_0} \right) + B_{_0} \mathbf{v}_E \cdot \left(\frac{n_{0\mathrm{e}}}{B_0} \right) - n_{0\mathrm{e}} \left(\mathbf{v}_{*\mathrm{e}} + \mathbf{v}_E \right) \cdot \frac{\nabla B_0}{B_0} = 0, \tag{9}$$

$$\frac{\partial n_\mathrm{i}}{\partial t} + B_{_0} \mathbf{v}_E \cdot \left(\frac{n_{0\mathrm{i}}}{B_0} \right) - n_{0\mathrm{i}} \mathbf{v}_E \cdot \frac{\nabla B_0}{B_0} = 0, \tag{10}$$

respectively.

For the ideal ballooning mode, we may assume that the mode complex frequency is much larger than the ion transit frequency ($|\omega| >> k_\parallel v_{T_\mathrm{i}}$) [20]. Then the ion current parallel to the magnetic field is much smaller than the electron parallel current, and can be ignored. Therefore, in deriving Eq. (10), similar terms as $v_{*\mathrm{e}}$ and $\delta u_{\parallel \mathrm{e}}$ appearing in Eq. (9) are neglected by assuming $T_\mathrm{i} = 0$ and a vanishing parallel ion cuurnt. Here, $n_{0\alpha} = \int \mathrm{d}\mathbf{v} f_{0\alpha}, n_\alpha = n_{0\alpha} + \delta n_\alpha$, with $\int \mathrm{d}\mathbf{v} \equiv (\pi B_0/m_\alpha) \int \mathrm{d}v_\parallel \mathrm{d}\mu$, and

$$\mathbf{v}_{*\mathrm{e}} = \frac{1}{n_{0\mathrm{e}} m_\mathrm{e} \Omega_\mathrm{e}} \mathbf{b}_0 \times \nabla \left(\delta p_{\perp \mathrm{e}} + \delta p_{\parallel \mathrm{e}} \right), \tag{11}$$

where $\delta p_{\perp \mathrm{e}} = \int \mathrm{d}\mathbf{v} \mu B_0 \delta f_\mathrm{e}$, $\delta p_{\parallel \mathrm{e}} = \int \mathrm{d}\mathbf{v} m v_\parallel^2 \delta f_\mathrm{e}$, with $\delta f_\mathrm{e} = f_\mathrm{e} - f_{0\mathrm{e}}$ being the perturbed part of the electron distribution function.

Applying the charge neutrality condition, and assuming a single dominant ion species, $n_{0\mathrm{i}} = n_{0\mathrm{e}}/Z_\mathrm{i}$, Eqs. (9) and (10) can be rewritten as

$$\frac{\partial \delta n_\mathrm{e}}{\partial t} + n_0 \mathbf{B}_0 \cdot \nabla \left(\frac{\delta u_{\parallel \mathrm{e}}}{B_0} \right) + \mathrm{v}_E \cdot \nabla n_0 - n_0 \mathbf{v}_* \cdot \frac{\nabla B_0}{B_0} - 2 n_0 \mathbf{v}_E \cdot \frac{\nabla B_0}{B_0} = 0, \tag{12}$$

$$\frac{\partial \delta n_\mathrm{i}}{\partial t} + \frac{1}{Z_\mathrm{i}} \mathbf{v}_E \cdot \nabla n_0 - \frac{2}{Z_\mathrm{i}} n_0 \mathbf{v}_E \cdot \frac{\nabla B_0}{B_0} = 0. \tag{13}$$

Here, we have abbreviated $n_{0\mathrm{e}}$ as n_0, and $\mathbf{v}_{*\mathrm{e}}$ as $\mathbf{v}_*$, respectively.

The electrostatic potential can be found from gyrokinetic Poisson's equation,

$$\frac{c^2}{4\pi e} \nabla_\perp \left(\frac{1}{v_\mathrm{A}^2} \nabla_\perp \delta \phi \right) = \delta n_\mathrm{e} - Z_\mathrm{i} \delta n_\mathrm{i}, \tag{14}$$

where v_A is the Alfven velocity and $\nabla_\perp = \nabla - \mathbf{b} \left(\mathbf{b} \cdot \nabla \right)$. Combining Eqs. (12)$\sim$(14), we get,

$$\frac{i\omega c^2}{4\pi e} \nabla_\perp \left(\frac{1}{v_\mathrm{A}^2} \nabla_\perp \delta \phi \right) + n_0 \mathbf{B}_0 \cdot \nabla \left(\frac{\delta u_{\parallel \mathrm{e}}}{B_0} \right) - n_0 \mathbf{v}_* \cdot \frac{\nabla B_0}{B_0} = 0. \tag{15}$$

The vector potential satisfies the gyrokinetic Ampere's law,

$$\frac{c}{4\pi} \left\{ \nabla \times \left[\left(\delta A_\parallel \mathbf{b}_0 \right) \right] \cdot \mathbf{b}_0 \right\} \mathbf{b}_0 = \sum_\alpha \delta \mathbf{J}_{\alpha \parallel}. \tag{16}$$

We neglect the $\delta B_\parallel = 0$ component of the magnetic field perturbation, so the vector potential has only the parallel component $\delta \mathbf{A} = \delta A_\parallel \mathbf{b}_0$, which is finally determined by the electron parallel fluid velocity $\delta u_{\parallel \mathrm{e}}$ by inverting the Ampere's law,

$$n_0 e \delta u_{\parallel \mathrm{e}} = \frac{c}{4\pi} \nabla_\perp^2 \delta A_\parallel. \tag{17}$$

We define an effective scalar potential ϕ_eff to represent the parallel electric field,

$$\delta E_\parallel = -\mathbf{b}_0 \cdot \nabla \delta \phi - \frac{1}{c} \frac{\partial \delta A_\parallel}{\partial t} = -\mathbf{b}_0 \cdot \nabla \delta \phi_\mathrm{eff}. \tag{18}$$

Then,

$$\frac{\partial \delta A_\parallel}{\partial t} = c \mathbf{b}_0 \cdot \nabla \delta \phi_\mathrm{ind}, \tag{19}$$

where we define the inductive potential $\delta \phi_\mathrm{ind} = \delta \phi_\mathrm{eff} - \delta \phi$.

By making the ideal MHD approximation, $\mathbf{b}_0 \cdot \nabla \delta \phi_\mathrm{eff} = 0$, and applying $\nabla_\perp^2$ operator on Eq. (19), we get,

$$\frac{1}{c} \frac{\partial}{\partial t} \left(\nabla_\perp^2 \delta A_\parallel \right) = -\mathbf{b}_0 \cdot \nabla \left(\nabla_\perp^2 \delta \phi \right). \tag{20}$$

Substituting Eqs. (17) and (20) into Eq. (15), we finally get

$$\frac{\omega^2}{v_\mathrm{A}^2} \nabla_\perp^2 \delta \phi + \mathbf{B}_0 \cdot \nabla \left[\frac{1}{B_0} \mathbf{b}_0 \cdot \nabla \left(\nabla_\perp^2 \delta \phi \right) \right] - \frac{8\pi e i \omega}{m_\mathrm{e} \Omega_\mathrm{e} c^2} \mathbf{b}_0 \cdot \kappa \times \nabla \delta p = 0, \tag{21}$$

where $\kappa = \nabla B_0 / B_0$ is the magnetic field curvature in a low beta case. Here, we have used the lowest order solution for the electron pressure $\delta p_{\perp \mathrm{e}}$ and $\delta p_{\parallel \mathrm{e}}$,

$$\delta p_{\perp \mathrm{e}} = \delta p_{\parallel \mathrm{e}} = \delta p = n_0 e \phi_\mathrm{eff}^0 + \frac{\partial \left(n_0 T_\mathrm{e} \right)}{\partial \psi_0} \delta \psi, \tag{22}$$

where ψ is the poloidal flux label, $\delta \phi_\mathrm{eff}^0$ is the lowest order effective potential $\delta \phi_\mathrm{eff}$ which is neglected in the ideal ballooning mode simulation. Linear normal mode theory ($\partial t \rightarrow -i\omega$, $\mathbf{b}_0 \cdot \nabla \rightarrow i k_\parallel$) is applied in the derivation. Eq. (21) is the eigenmode equation for the ideal ballooning mode derived from electromagnetic gyrokinetic formalism. It recovers the ideal MHD ballooning equation in Ref. [20], which shows that with the kinetic effects turned off and in the long wavelength limit, the gyrokinetic formulation can be reduced to the ideal MHD theory. Therefore, the present fluid-kinetic hybrid electron model is a superset of the ideal MHD theory. More complete eigenmode equations including the kinetic ballooning mode and current-driven kink modes can be found in Ref. [12].

3 Simulation results and discussion

In this section, we describe results of GTC simulations of the ideal ballooning mode and compare them with the results of the BOUT++ code [2,21]. BOUT++ is an adaptable, object-oriented C++ code for performing parallel plasma fluid simulations with an arbitrary number of equations in 3D curvilinear coordinates using finite-difference methods. For the purpose of comparison with BOUT++ simulation we artificially suppress the kinetic effects of electrons and ions in the GTC simulation of ideal ballooning modes.

The edge localized ballooning instabilities can be driven by the large pressure gradient at the pedestal region. Here, for comparison and benchmarking, we adopt the same pedestal pressure and safety factor profiles as those of Refs. [1, 2], shown in Fig. 1 and Fig. 2, respectively. The maximum pressure gradient occurs at about about $\psi = 0.7\psi_{\rm wall}$, with ψ being the poloidal magnetic flux function, and $\psi_{\rm wall}$ is the maximun value of ψ. In the simulation, we use an initial perturbation in $\delta n_{\rm e}$,

$$\delta n_{\rm e} = \delta\hat{n}_{\rm e} \sum_m m^2 \exp^{-2|nq-m|} \cos\left(m\theta - n\zeta\right), \qquad (23)$$

where $\delta\hat{n}_{\rm e}$ is amplitude of the initial perturbation, q is the safety factor, m and n are poloidal and toroidal mode numbers, respectively, with $m = nq$ at the mode rational surfaces. In the GTC we use toroidal magnetic coordinates, which are poloidal magnetic flux function ψ, poloidal angle θ, and toroidal angle ζ.

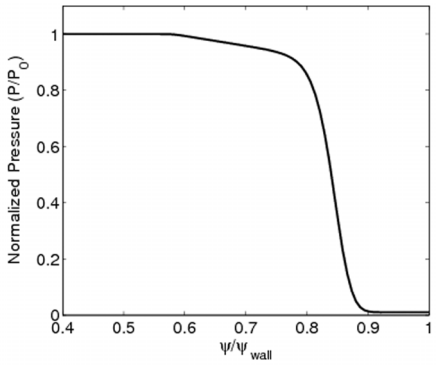

Fig.1 Pedestal pressure profile as a function of the normalized poloidal magnetic flux ψ

We start with the convergence test for spatial and temporal resolution. The results are shown in Fig. 3. We can see that convergence requires about 28 poloidal grid points per wavelength. The time step convergence is also achieved throughout the simulations.

The results of the GTC simulations of the ideal ballooning mode are presented in Figs. 4∼7, where we show the poloidal contour plots of the electrostatic potential ($\delta\phi$) and the parallel component of the magnetic vector potential ($\delta A_{\parallel}$) for toroidal mode number n = 10, 20, and 30, respectively. As we can see from the contour plots in Figs. 5∼7, the mode has a clear ballooning structure localized on the outer side of the poloidal cross section, similar for different toroidal mode numbers. The radial localization occurs at the region of the maximum pressure gradient, as shown in Figs. 1 and 4. The magnetic vector potential has only interchange parity near the mode rational $\delta A_{\parallel}$ surface, since the tearing mode parity is excluded in the fluid-kinetic hybrid electron model currently implemented in the GTC [11].

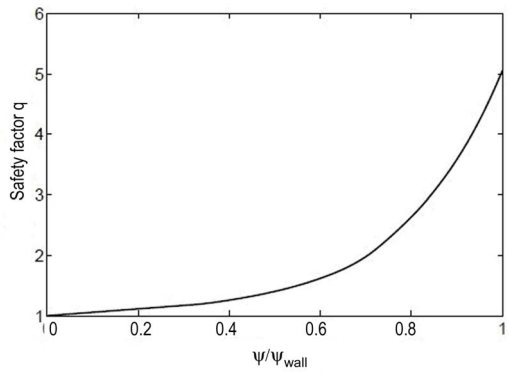

Fig.2 Safety factor profile as a function of the normalized poloidal magnetic flux ψ

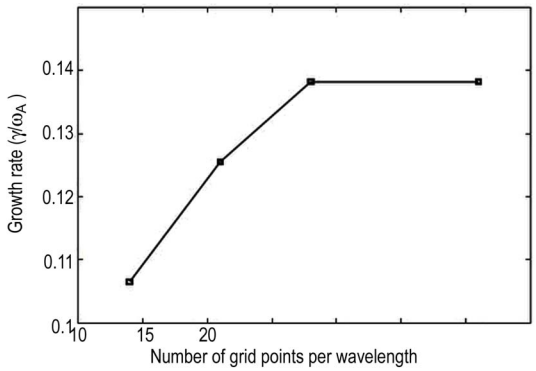

Fig.3 Spatial convergence test, with $n = 15$. Growth rate γ increases with the number of grid points per wavelength. Spatial convergence is achieved when the number of grid points per wave-length exceeds 28

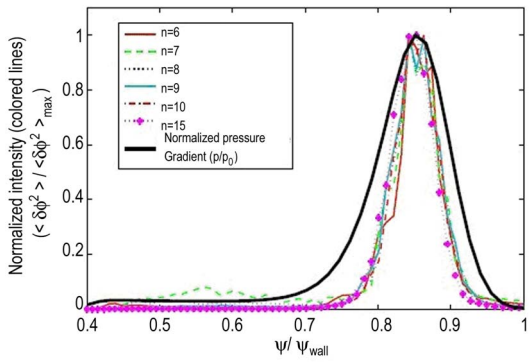

Fig.4 Normalized electrostatic potential intensity (colored lines) and normalized pressure gradient (black line), as a function of the normalized poloidal magnetic flux ψ (color online)

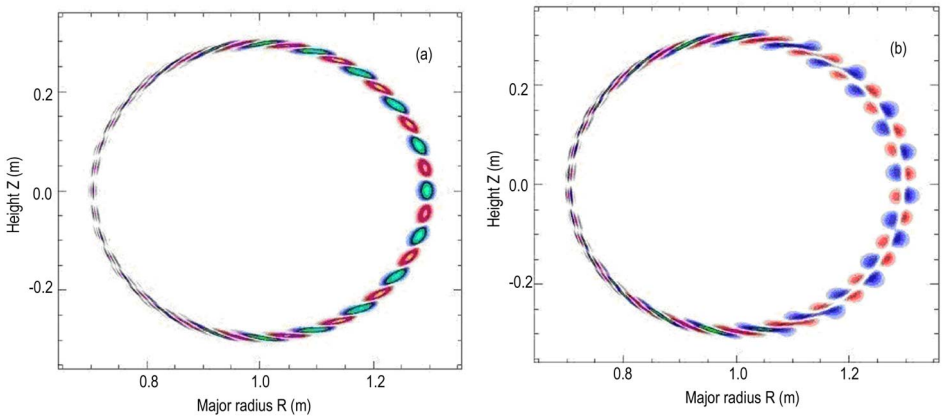

Fig.5 GTC simulation of ideal ballooning modes: contour plots of the poloidal eigenmode structure of (a) the electrostatic potential $\delta\phi$, and (b) the parallel vector potential $A_{\|}$ for toroidal mode number of $n = 10$ (color online)

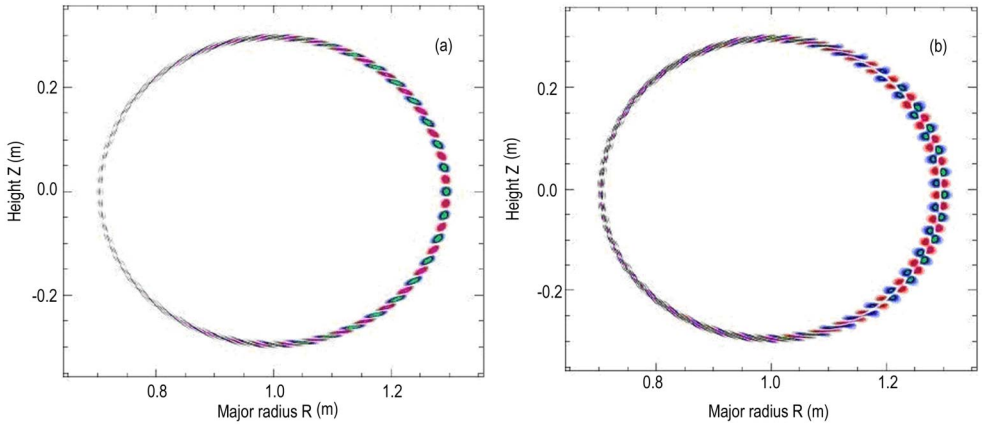

Fig.6 GTC simulation of ideal ballooning modes: contour plots of the poloidal eigenmode structure of (a) the electrostatic potential $\delta\phi$, and (b) the parallel vector potential $A_{\|}$ for toroidal mode number of $n = 20$ (color online)

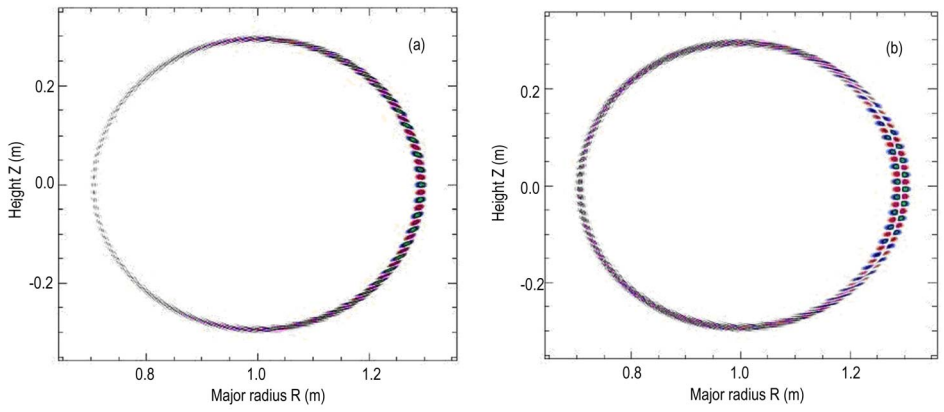

Fig.7 GTC simulation of ideal ballooning modes: contour plots of the poloidal eigenmode structure of (a) the electrostatic potential $\delta\phi$, and (b) the parallel vector potential $A_{\|}$ for toroidal mode number of $n = 30$ (color online)

The typical mode structure of the electrostatic potential on the magnetic surface is shown in Fig. 8. Here $\alpha = q(\psi)\theta - \zeta$ is the magnetic field line label. We can see that the ballooning mode is highly elongated in the parallel direction. The poloidal profile of root mean square (RMS) value of the electrostatic potential is given in Fig. 9, with the horizontal axis being the poloidal angle θ ranges from 0 to 2π .

The ballooning mode structure obtained in GTC simulations is similar to that obtained in simulations

using BOUT++ and several other MHD codes [21,22]. The minor difference between mode structures of GTC and the fluid codes (see Fig. 11 in Ref. [21]) can be explained by the different equilibrium geometry: in the current GTC simulations we use circular magnetic poloidal cross section, while the fluid codes use elongated poloidal cross section.

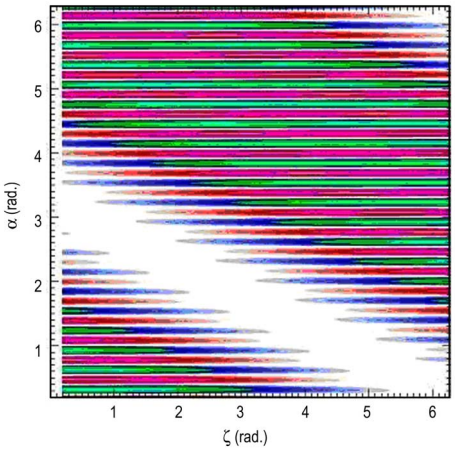

Fig.8 The mode structure of the electrostatic potential on a magnetic surface, with $n = 10$ (color online)

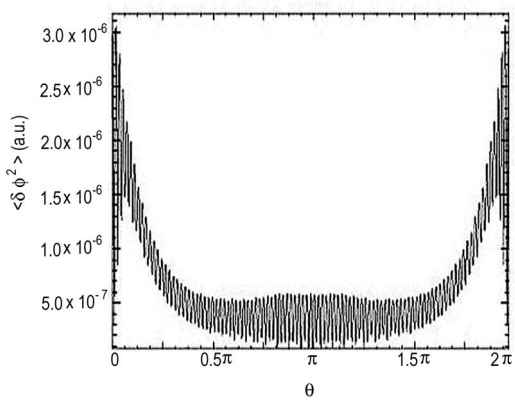

Fig.9 The poloidal profile of the RMS value of electrostatic potential

The growth rate dependency on the toroidal mode number n is shown in Fig. 10. Here, the growth rate γ is normalized to the Alfven frequency $\omega_A = v_A/R$, with v_A the Alfven velocity and R the major radius. We can see that the ideal ballooning mode is unstable for the toroidal mode number from $n = 3$ to 30, for the given set of equilibrium parameters. In the simulation we begin with the initial perturbation in the form of Eq. (23), then the plasma undergoes a transient phase and finally settles on an eigenmode with a single growth-rate, as shown in the inset of Fig. 10, where we also plot the time evolution of the amplitude of electrostatic potential. The slope of the time evolution curve gives the growth rate γ of ideal ballooning mode, as indicated by the red-dash line in the inset. The growth rate of the ideal ballooning mode instability is increased with increasing n, which is consistent with the result of linear MHD simulations [22].

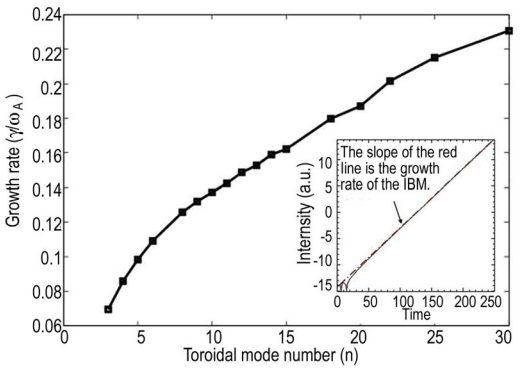

Fig.10 Growth rate γ of ideal ballooning mode instability as a function of the toroidal mode number n. The inset: time history of the amplitude, the slope of the time evolution curve gives the growth rate γ

4 Conclusion

We have performed simulations of the ideal ballooning mode using global gyrokinetic toroidal code GTC. Excitation of the ideal ballooning mode instability is observed in the region of the maximum pressure gradient. The linear mode structure is similar to the mode structure obtained in the fluid simulations, while the scaling of the linear growth rate with the toroidal mode number is consistent with the ideal MHD theory. Our studies confirm the ability of GTC to simulate MHD types of instabilities. In future work we are going to include kinetic effects to address the wave-particle interactions and other related physical phenomena.

Acknowledgments

We acknowledge fruitful discussions with Xueqiao XU, who provides the equilibrium data of Figs. 1 and 2. Simulations were performed using supercomputers at NERSC.

References

1 Xu X Q, Nevins W M, Cohen R H, et al. 2002, New J. Phys., 4: 53
2 Xu X Q, Umansky M V, Dudson B, Snyder P B. 2008, Commun. Comput. Phys., 4: 949
3 Rowan W L, Meigs A G, Austin M E, et al. 1989, Bull. Am. Phys. Soc., 34: 2152
4 Zarnstorff M C, McGuire K, Bell M G, et al. 1990, Phys. Fluids B, 2: 1852
5 Lau Y T. 1990, Nucl. Fusion, 30: 934
6 McCarthy D F L, Guzbar P N, Drake J F, et al. 1992, Phys. Fluids B, 4: 1846
7 Snyder P B, Groebner R J, Leonard A W, et al. 2009, Phys. Plasmas, 16: 056118
8 Connor J W, Hastie R J, Wilson H R, et al. 1998, Phys. Plasmas, 5: 2687
9 Lee W W. 1983, Phys. Fluids, 26: 556
10 Lin Z, Hahm T S, Lee W W, et al. 1998, Science, 281: 1835

11 Holod I, Zhang W L, Xiao Y, et al. 2009, Phys. Plasmas, 16: 122307
12 Deng W, Lin Z, Holod I. 2012, Nuclear Fusion, 52: 023005
13 Zhang H S, Lin Z, Holod I, et al. 2010, Phys. Plasmas, 17: 112505
14 Deng Wenjun, Lin Zhihong, Holod Ihor, et al. 2010, Phys. Plasmas, 17: 112504
15 Zhang Wenlu, Holod Ihor, Lin Zhihong, et al. 2012, Phys. Plasmas, 19: 022507
16 Brizard A J, Hahm T S. 2007, Rev. Mod. Phys., 79: 421
17 Nishimura Y, Lin Z, Wang W X. 2007, Phys. Plasmas, 14: 042503
18 Lin Z, Chen L. 2001, Phys. Plasmas, 8: 1447
19 Lin Z, Nishimura Y, Xiao Y, et al. 2007, Plasma Phys. Controlled Fusion, 49: B163
20 Hazeltine R D, Meiss J D. 2003, Plasma Connement. Courier Dover Publications, New York
21 Dudson B D, Umansky M V, Xu X Q, et al. 2009, Computer Physics Communications, 180: 1467
22 Burke B J, Kruger S E, Hegna C C, et al. 2010, Phys. Plasmas, 17: 032103

(Manuscript received 20 February 2012)
(Manuscript accepted 10 July 2012)
E-mail address of LI Zebin: lizebin.xm@163.com